Datashare 114A

Nuclear magnetic resonance and x-ray microtomography pore-scale analysis of oil recovery in mixed-porosity carbonates

Hubert King, Michael Sansone, John Dunsmuir, Nicole Callen, Pavel Kortunov, Ye Xu, Antonio Buono, Bo Gao, and James Kralik

AAPG Bulletin, v. 104, no. 1 (January 2020), pp. 37–52

LOW- AND HIGH-FIELD NUCLEAR MAGNETIC RESONANCE ANALYSIS

Methodology

We developed two nuclear magnetic resonance (NMR)-based techniques to simultaneously study static and dynamic properties of microcarbonate rocks (Figures SA1, SA2). These techniques allow for (1) direct measurement of the total amount of oil and water in the rock sample and total porosity, (2) estimation of micro- and macropores fractions, (3) measurement of core-scale fluid flow, (4) monitoring of mechanisms of oil recovery, (5) and through an in situ fluid-handling system, simultaneous measurement of rock permeability.

Low-Field In Situ Nuclear Magnetic Resonance

The first experimental setup is based on several low-field NMR instruments (0.047 T or 2 MHz on ^{1}H) coupled with custom pressure cells that allow running fluid saturation and flow experiments at reservoir conditions with confining pressures up to 700 bar, a pore pressure up to 700 bar, and a sample temperature up to 150°C on 1-in. and 1.5-in. outer diameter standard core plugs (Figure SA1). It is worth noting that NMR signal at low-field provides a total ^{1}H content of water and oil and does not allow for the separation of water and oil signals.

To visualize an oil recovery with low-field NMR, we use deuterated water D_2O (which is undetectable by ^{1}H NMR) and a natural oil detectable by ^{1}H NMR. For water visualization, fluorinated synthetic oil can be used as a surrogate for natural oil. The key features and applications of a low-field NMR setup are

- total porosity with oil and/or water saturated sample (^{1}H signal)
- fractions micro- and macropores (T_2 relaxometry)
- potential for wettability (T_1-T_2 relaxometry)
- custom fluid flow system at reservoir conditions up to 700 bar and 150°C
- one-dimensional (1-D) visualization of oil recovery
- measurements of a sample permeability
- applied to shale gas and carbonates
- low sensitivity to magnetic impurities (e.g., pyrite)

High-Field In Situ Nuclear Magnetic Resonance–Magnetic Resonance Imaging

The second experimental setup is based on a high-field NMR spectrometer (9.4 T or 400 MHz on ^{1}H) and offers a spectroscopic separation of oil and water signals in the rock sample as well as 1-D and three-dimensional (3-D) imaging of either oil or water in the rock up to 1 in. in diameter (Figure SA2) (provided that the sample has low concentrations of ferromagnetic minerals). Tight space inside a magnetic resonance imaging (MRI) probe of 30 mm restricts options to build a cell for experiments at high pressure. The key features and applications of a high-field NMR–MRI setup are

- total oil and water saturation, total porosity (^{1}H spectroscopy)
- fractions of oil/water in micro- and macropores (T_2 relaxometry)
- potential for wettability (T_1-T_2 relaxometry)
- custom fluid flow system at low pressure up to 5 bar
- 1-D visualization of oil recovery and water flow in the sample
- 3-D maps of oil and water
- measurements of a sample permeability
- high sensitivity to magnetic impurities (e.g., pyrite)

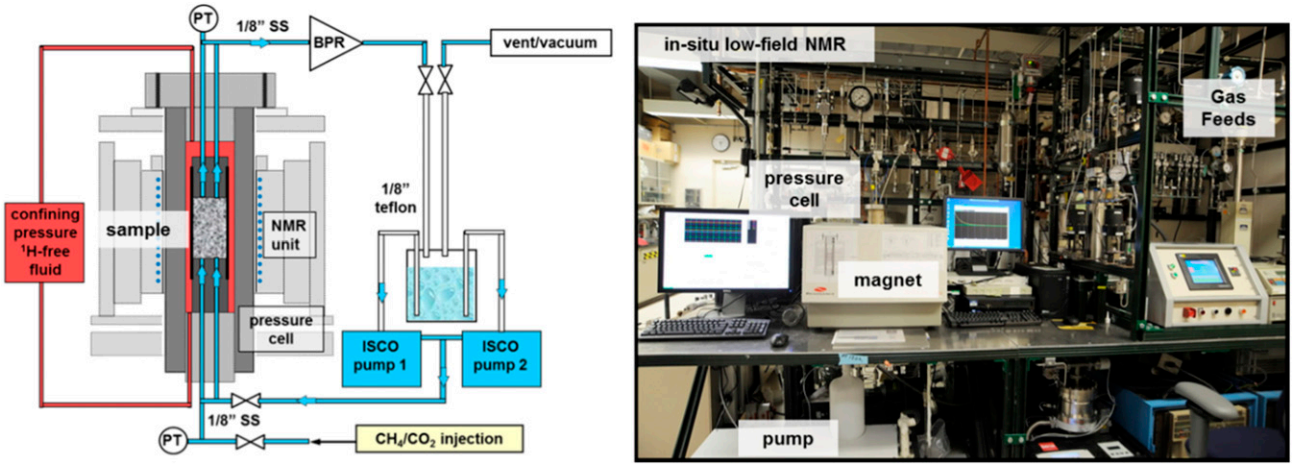

Figure SA1. Schematic of a low-field in situ nuclear magnetic resonance (NMR) setup to study a fluid saturation and flow in rocks at low spatial resolution and reservoir conditions up to 700 bar and 150°C. BPR = back pressure regulator; ISCO = Teledyne ISCO Syringe Pump; PT = pressure transducer; SS = stainless steel tubing.

Pulsed Field Gradient Nuclear Magnetic Resonance for Flow Measurements

Both low- and high-field NMR setups are equipped with pulsed field gradient (PFG) coils, which enable measurements of the translational movement of molecules within the sample. The PFG NMR technique detects an average mean square displacement $\langle \Delta z^2 \rangle$ of the entire ensemble of molecules during an observation time t_{obs}, which leads to calculations of an actual pore-scale fluid flow in the sample. In addition to an average fluid flow, the technique can provide a distribution of fluid flows and define a fraction of a stationary fluid.

Detection of Oil and Water with ^{1}H Spectroscopy

The NMR is a direct and noninvasive technique to quantitatively measure the amount of fluid in the rock. Whereas low-field NMR detects total signal from hydrogen containing fluids under observation, high-field NMR differentiates signals from different fluids such as oil (e.g., -C<u>H</u>) and water (e.g., -O<u>H</u>) based on different chemical environment and, therefore, resonance frequencies of hydrogen nuclei. Combined volume of oil and water referenced against a core-plug volume also gives a total fluid-filled porosity of the core plug.

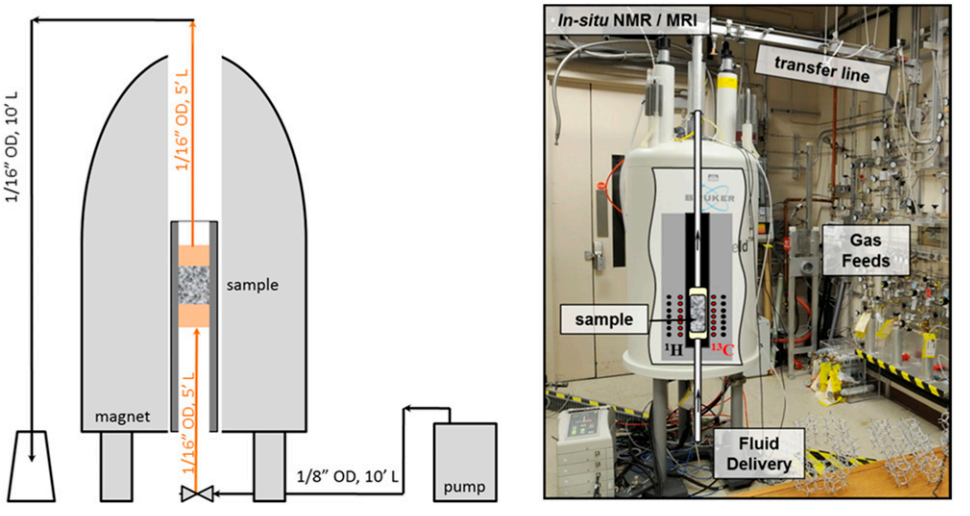

Figure SA2. Schematic of a high-field in situ nuclear magnetic resonance (NMR)–magnetic resonance imaging (MRI) spectrometer to study a fluid saturation and flow in rocks at high spatial resolution and low pressures below 5 bar. OD = outer diameter of tubing.

We applied high-field NMR spectroscopy to measure oil and water content in carbonate samples as received from the field, after saturation with oil, after brine flood, and after storage in brine for a few months.

Figure SA3 shows an example of a typical ^{1}H NMR spectra of a produced oil (left) and oil–water saturated plug (right). Natural oil gives two general types of ^{1}H resonances: hydrogen atoms attached to aromatic carbons at 6.0–8.0 ppm = C(H)- and hydrogen atoms attached to aliphatic carbons -C(H_x)- at 0.5–2.0 ppm (Figure SA3, left). The NMR signal from water (Figure SA3, right) is commonly found at 4.5–5.0 ppm, which allows for the separation of the water signal from the oil signal.

We tested several approaches to quantify NMR signal and compute actual amount of water and oil from ^{1}H NMR spectrum. The first approach was to quantify the oil amount based on the H/C ratio of aromatic and aliphatic components. The second approach was based on the fitting of the complex ^{1}H NMR spectrum with several Gaussian components, which represent aromatic oil, aliphatic oil, and water signals. The latter approach gave meaningful results with a large error because of nonsymmetrical experimental peaks (see Figure SA3, left).

The best approach to quantifying ^{1}H NMR signal from the core plug is to directly fit the entire experimental spectrum from the core plug (such as Figure SA3, right) with broadened and weighted experimental spectra of known amounts of bulk oil (such as Figure SA3, left) and known amounts of bulk brine (not shown here) measured on the same experimental setup at the same experimental conditions. Here, we report quantitative analysis based on such an approach with four reference samples: 0.992 g of crude oil dissolved in d8-toluene (invisible for ^{1}H NMR), 1.022 g and 2.032 g of brine in D_2O, and 2.030 g of seawater in D_2O with total volumes of each reference sample similar to a core-plug volume (~13.0 cm^3).

Traditional fluid analysis based solely on T_2 relaxation of fluids measured by low-field NMR is challenged by identification and quantification of components reflecting signals from water and oil. Figure SA4 compares the ^{1}H NMR spectrum of oil-saturated sample 2 measured by high-field NMR spectrometer (left) and conventional T_2 spectrum measured with low-field NMR instrument (right). Whereas ^{1}H NMR spectroscopy clearly detects and quantifies a brine (taking into account the characteristic resonance frequency of water) and oil, analysis of low-field T_2 spectrum showing four components is more challenging as it reflects oil and brine in different pore systems.

Figure SA5 shows the ^{1}H NMR spectra of a microporous sample 1 after oil saturation and after a brine flood. Oil-saturated sample 1 contains a small

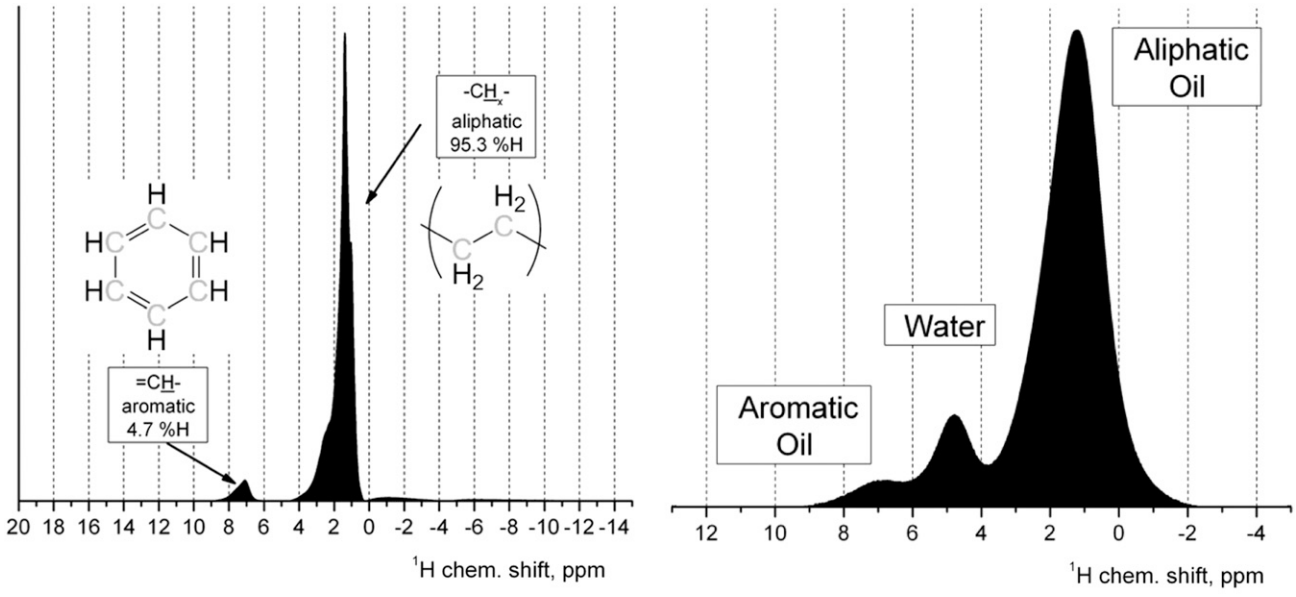

Figure SA3. The ^{1}H nuclear magnetic resonance spectra of a bulk oil (left) and oil-saturated core plug sample 2 (right) measured with a 30-mm (1.2 in.) magnetic resonance imaging probe. Aromatic and aliphatic oil components are shown at 6.0–8.0 ppm and 0.5–2.0 ppm, respectively. Horizontal axis is proton chemical (chem.) shift.

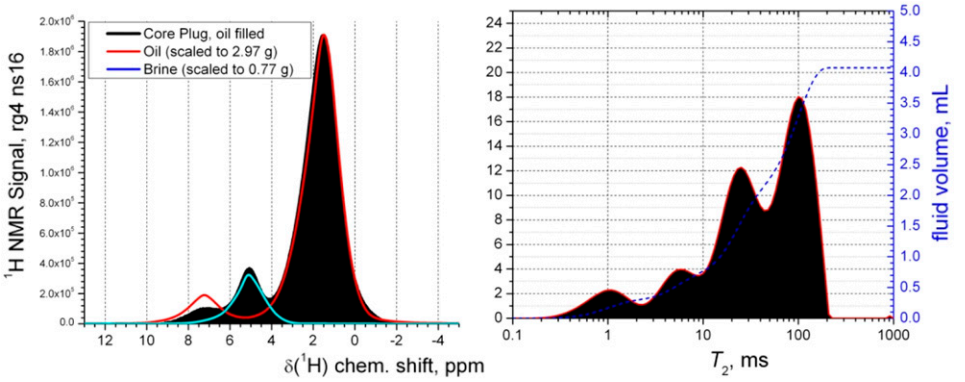

Figure SA4. The ^{1}H nuclear magnetic resonance (NMR) spectrum (left) and spin–spin relaxation time (T_2) spectrum (right) of oil-saturated sample 2 measured with high- and low-field NMR instruments, respectively. chem. = chemical.

amount of residual brine (~0.14 g or 1.0 sample volume [BV%]), whereas the majority of the ^{1}H signal is detected from 2.12 g of oil to give 19.5 BV% oil-filled porosity, resulting in a total fluid-filled porosity of 20.5 BV%. Brine flood experiments produced approximately 54% of the initially stored oil reducing an oil-filled porosity from 19.5 to 9.0 BV%. Brine flood led to a much stronger brine signal equivalent to 1.81 g of brine to give a brine-filled porosity of 12.9 BV% and a total plug porosity (oil + brine) of 21.9 BV%.

Figure SA6 shows low-field T_2 spectra of sample 1 before oil saturation (left) and after brine flood (right). As the oil-filled sample has a low concentration of remaining brine (Figure SA5, left), Figure SA6 (left) shows the complex relaxation behavior of oil molecules in sample 1. Three T_2 peaks may show relaxation of different fractions of oils (higher versus lower molecular weight) as well as fraction of molecules reaching the surface and remaining in the pore interior during the experiment. Although one can identify a new T_2 component at 200–600 ms (Figure SA6, right for brine-flooded sample), which likely reflects brine, it still remains challenging to accurately define components responsible for oil and brine over the T_2 range between 5 and 100 ms. Brine in micropores may have T_2 values overlapping with T_2 values of oil in macropores at T_2 of approximately 50–100 ms. The T_1-T_2 correlation experiments did not provide additional separation of oil and brine signals as T_1/T_2 ratio of all detected components is approximately 2:1.

Determination of Macro- and Microporosity

Relative fraction of fluid-filled micro- and macropores can be estimated with NMR by monitoring the

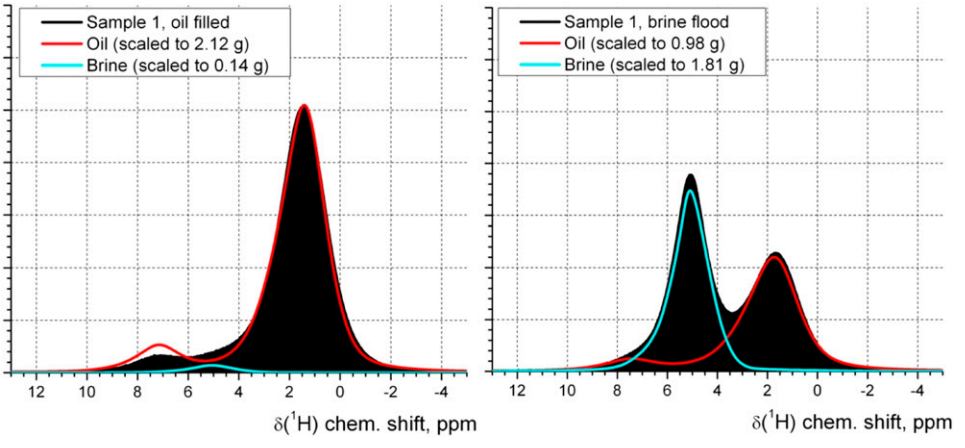

Figure SA5. The ^{1}H nuclear magnetic resonance (NMR) spectra of sample 1 saturated with oil (left) and after brine flood (right) measured with high-field NMR spectrometer. Red and blue lines show broadened and weighted spectra of bulk oil and bulk brine used for oil and brine quantification. chem. = chemical.

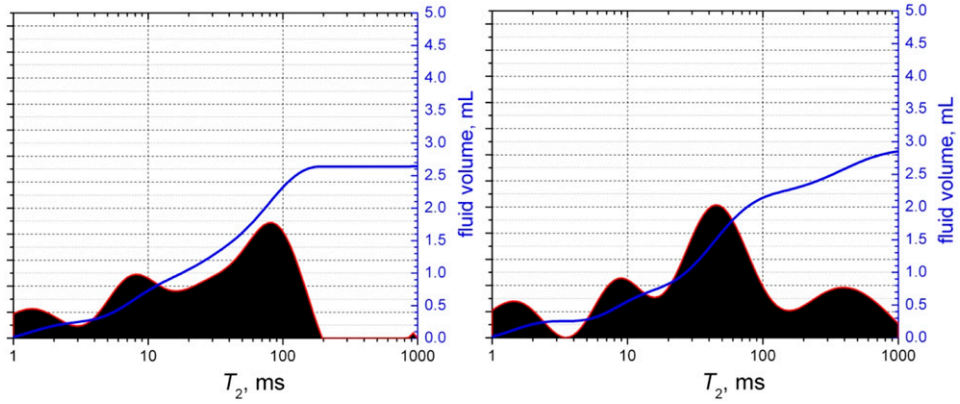

Figure SA6. The spin–spin relaxation time (T_2) spectra of a core plug similar to sample 1 saturated with oil (left) and after brine flood (right) measured with low-field nuclear magnetic resonance instrument. Quantification of guest brine and remaining oil is challenging.

rate of an NMR signal decay (e.g., T_2 relaxation), which is shorter for a high rate of guest–host collisions (e.g., smaller pores or surface layer) and longer for a low rate of guest-host collisions (e.g., larger pores). In addition to a standard T_2 relaxometry, high-field NMR offers a chemically resolved T_2 relaxometry, which allows for separately probing a pore environment of oil and brine based on relaxation rates of individual components. Relative fractions of micro- and macropores determined from T_2 relaxometry combined with a total amount of oil by ^{1}H NMR spectroscopy allows for quantifying the amount of oil in micro- and macropores.

Figure SA7 shows T_2 relaxation decays of oil and water and brine in microporous sample 1. The ^{1}H NMR signal from aliphatic oil (peak at 1.5 ppm) of an oil-filled sample decays with two rates—95% of hydrogen protons relax with T_2 = 1.65 ms, whereas the remaining 5% of oil relaxes with a longer T_2 = 5.1 ms (Figure SA7, left). Assuming 0.13 cm^3 or 5 pore volume (PV%) of detected brine (Figure SA5, left) is similarly distributed, we define 95 PV% as a percent of micropores in sample 1.

A brine flood led to displacement of oil from macropores as a fraction of longer relaxing oil component reduces from 5% to 1% (Figure SA7, right), whereas 99% of remaining oil is located in micropores with shorter T_2 of 1.3 ms.

Figure SA8 shows the ^{1}H NMR spectra of sample 2 (mixed-porosity carbonate) after oil saturation (left)

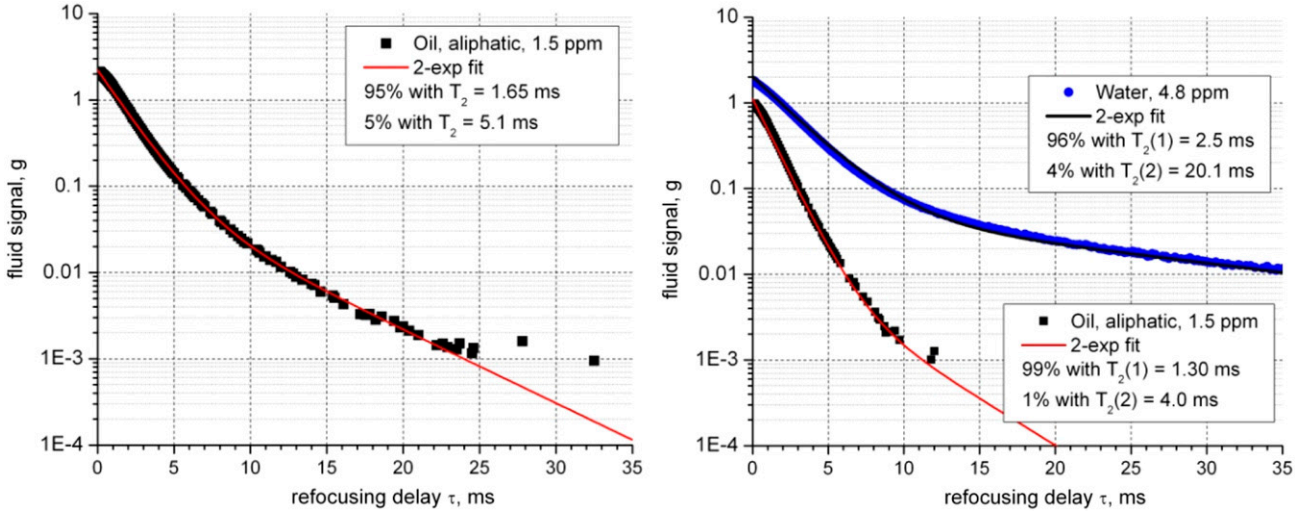

Figure SA7. The spin–spin relaxation time (T_2) relaxation decays of oil and brine in sample 1 saturated with oil (left) and after brine flood (right) measured with high-field nuclear magnetic resonance spectrometer. Red lines show the fit of experimental data used for quantification of oil fraction in micropores (shorter T_2) and macropores (longer T_2). exp = exponential.

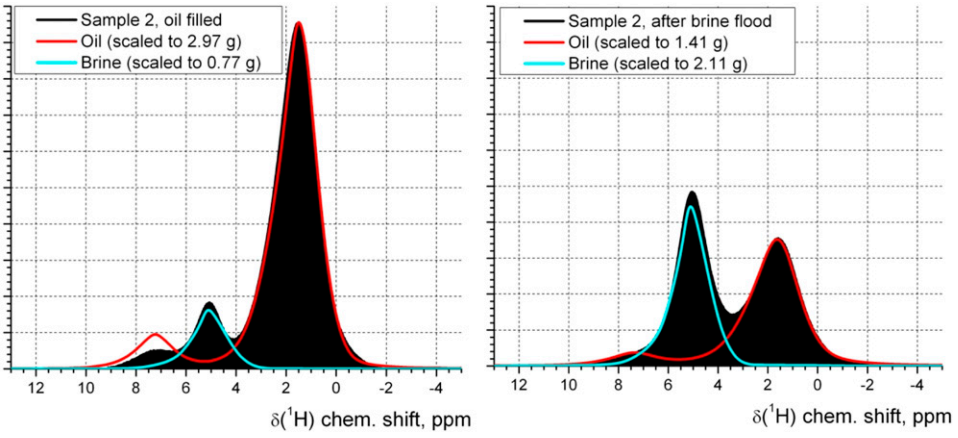

Figure SA8. The ^{1}H nuclear magnetic resonance (NMR) spectra of sample 2 saturated with oil (left) and after brine flood (right) measured with high-field NMR spectrometer. Red and blue lines show broadened and weighted spectra of bulk oil and bulk brine used for oil and brine quantification. chem. = chemical.

and after a brine flood (right). After oil saturation and initial measurements (Figures SA8, left, SA9, left, SA10, left), sample 2 was shortened from 33.0 to 28.3 mm to better fit detection volume of computerized tomography instrument. Reduction of sample length led to reduction of sample volume from 16.85 to 14.45 cm^3. Brine flood experiments and following NMR characterization was performed on a shorter 14.45 cm^3 sample 2.

In contrast to a microporous sample 1, oil-filled sample 2 contained a higher brine-filled porosity of approximately 4.1 BV% and higher total fluid-filled porosity of 24.8 BV% upon oil saturation. Brine flood experiments produced only 44% of the initially stored oil, reducing an oil-filled porosity from 20.7 to 11.5 BV%. Oil recovery from mixed-porosity sample 2 is smaller than that from the microporous sample 1.

Figure SA9 shows the low-field T_2 spectra of sample 2 after oil saturation (left) and after brine flood (right). It remains challenging to define components responsible for oil and brine at each phase of saturation. Therefore, quantification of oil and brine from T_2 measurements is not feasible. Because T_2 time of oil in fully oil-saturated sample 2 covers the range of 1–100 ms (Figure SA9, left), we anticipate that the new T_2 component at 300–2000 ms represents brine in macropores (Figure SA9, right). Brine in micropores may have T_2 values overlapping with T_2 values of oil in macropores at T_2 of approximately 50–100 ms. The T_1-T_2 correlation experiments did not provide additional separation of oil and brine signals as T_1/T_2 ratio of all detected components is approximately 2:1.

Figure SA10 shows T_2 relaxation decays of oil and water and brine in mixed-pore sample 2. The

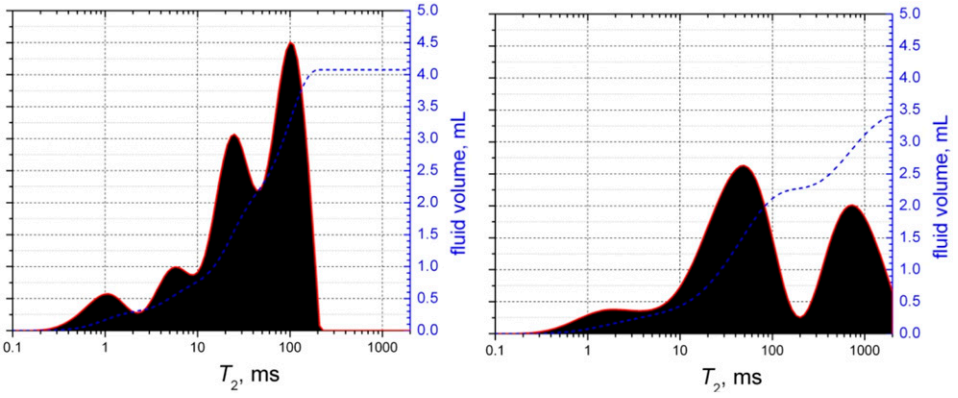

Figure SA9. The spin–spin relaxation time (T_2) spectra of sample 2 saturated with oil (left) and after brine flood (right) measured with low-field nuclear magnetic resonance instrument. Quantification of guest brine and remaining oil is challenging.

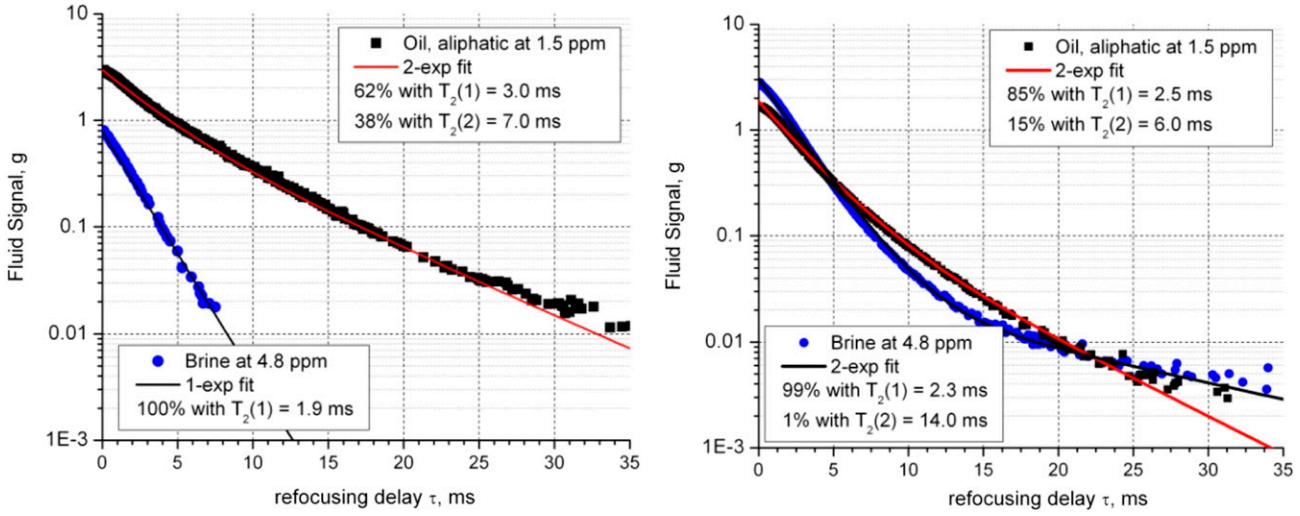

Figure SA10. The spin–spin relaxation time (T_2) relaxation decays of oil and brine in sample 2 saturated with oil (left) and after brine flood (right) measured with high-field nuclear magnetic resonance spectrometer. Red lines show the fit of experimental data used for quantification of oil fraction in micropores (shorter T_2) and macropores (longer T_2). exp = exponential.

^{1}H NMR signal from aliphatic oil (peak at 1.5 ppm) of an oil-filled sample decays with two rates–62% of hydrogen protons relax with T_2 = 3.0 ms, whereas the remaining 38% of oil relaxes with a longer T_2 of 7.0 ms (Figure SA10, left). Assuming 0.77 cm^3 or 16.5 PV% of detected brine (Figure SA8, left) is distributed similarly, we define 68 PV% as a percent of micropores in sample 2.

A brine flood led to a displacement of oil from macropores as a fraction of longer relaxing oil component reduces from 38% to 15% (Figure SA10, right), whereas 85% of remaining oil is located in micropores.

It is worth noting the difference in T_2 values of oil in micropores of samples 1 and 2 of 1.65 and 3.00 ms, respectively (Figures SA7, SA10, left). As T_2 relaxation mechanism reflects confinement, one could assume that micropores of sample 1 are smaller than micropores of mixed-porosity sample 2. However, a larger amount of detected brine in oil-saturated sample 2 (Figure SA8) could also reflect the presence of a water layer on the micropore surface of sample 2 that changes relaxation of oil present in the center of micropores. Detailed study of the relaxation times related to micropore size and water content is underway.

Nuclear magnetic resonance and x-ray microtomography pore-scale analysis of oil recovery in mixed-porosity carbonates

Hubert King, Michael Sansone, John Dunsmuir, Nicole Callen, Pavel Kortunov, Ye Xu, Antonio Buono, Bo Gao, and James Kralik

AAPG Bulletin, v. 104, no. 1 (January 2020), pp. 37–52

XENON LABELING OF OIL FOR X-RAY MICROTOMOGRAPHIC IMAGING AND SATURATION PROCEDURES FOR CORE PLUGS

Xenon Solubility in Oil

Xenon has a high solubility in hydrocarbon phases and very limited solubility in water. This, along with the high x-ray attenuation of xenon, makes it an excellent tagging agent for fluids in rocks.

The solubility of xenon has been reported for two typical oils: heavy and light (Potter and Clynne, 1978; Kharaka and Specht, 1988). These authors measured the solubility and related this to temperature and gas fugacity through solubility constants. Taking these constants, we can interpolate them to the conditions of our experiments for these two oils and compare them with that of our oil A.

We start by first measuring the solubility of xenon in oil A at a selected temperature and pressure. Using a pressurized fluid holder, we determined the x-ray attenuation of the oil with and without xenon pressure. A similar determination is made of the gas. The linear attenuation coefficient change is 1.244 and 0.631 cm^{-1}, respectively. The ratio of attenuation for oil-to-gas is a direct measure of the molar concentration between the two phases. Using the calculated molar volume of xenon gas, 336.6 mol/m^3 at these conditions, we obtain the concentration of xenon in oil A as 663.6 mol/m^3. We now compare this value with those previously reported for heavy and light oils in Figure SB1.

We now use the solubility constants for heavy and light oil to calculate the pressure dependence of xenon concentration. A relationship between fugacity (F) and pressure (P) and temperature (T) is used, $F = P + 9T_cP^2/128TP_c \times 1 - 6T_c^2/T_c$, where the critical temperature and critical pressure, respectively, for xenon are T_c = 16.59 C and P_c = 59.2 psi. In Figure SB2, the resulting calculations for oil A are compared to those for heavy and light oil from Khara and Specht (1988).

Linear X-Ray Absorption Coefficients

As an example of the relative attenuation of the components in a typical rock, we use the above equations and an assumption of an effective x-ray energy to calculate the linear attenuation coefficients. In Figure SB3, the attenuation of brine and oil are compared to that of calcite.

Transport through the Water Phase

Having established that xenon is highly soluble in oil and sparingly soluble in water, we now consider the transport of xenon into the core plug, which will contain both.

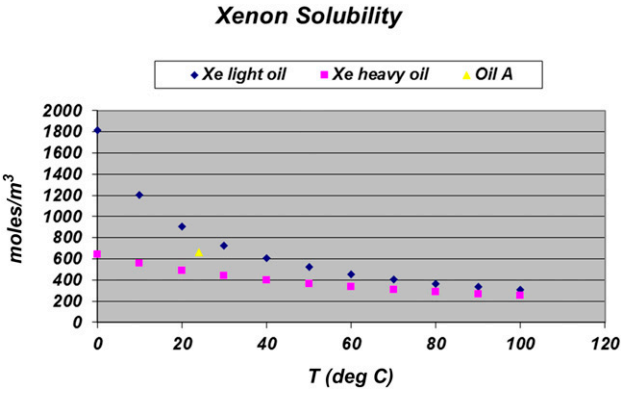

Figure SB1. Oil A xenon concentration lies between the heavy and light oils reported by Kharaka and Specht (1988).

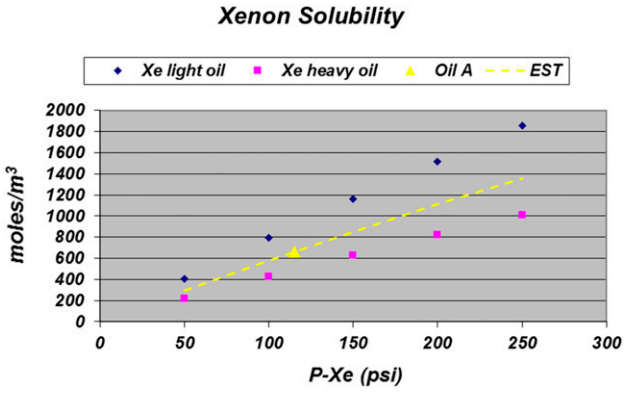

Figure SB2. Xenon concentration versus pressure is compared for heavy and light oils from Kharaka and Specht (1988). Also shown is the interpolation used in describing the predicted oil A dependence (EST). This approximation is made using the assumption that the concentration ratio oil A/(light oil – heavy oil) is pressure independent.

The uptake rate of xenon into the oil is governed by diffusion, with a rate well approximated by the diffusion coefficient calculated by the Stokes–Einstein approximation. We verified experimentally that this is rapid. The second question concerns water as a factor. With xenon transport through water expected to be also governed by diffusion, will the low solubility significantly impede oil saturation? Our first tests were made using a water-saturated membrane with a thickness of 0.25 mm (0.01 in.), and we found that the gas uptake rate of the oil was unaffected. For the next tests we used a several-centimeter-long capillary tube with 4.2-mm (0.17 in.) internal diameter. The bottom third of the tube was filled with wax, the middle third with water, and the top was empty. Wax was used to avoid the problem of buoyancy, which would have brought the oil to the top of the water. The tube was mounted inside a pressure vessel on the x-ray microtomography (XMT) unit. Using a fixed xenon gas pressure and time-dependent x-ray attenuation measurements, we then monitored the xenon concentration in the water and wax phases. The results are summarized in Figure SB4.

Transport into the Porous Rock Core Plug

Because we wish to avoid any fluid movement within the core plug prior to brine flooding, saturating the core-plug oil with xenon requires some careful management of pressures and volumes of the phases. The starting point for each experiment is an oil-saturated core plug, saturated externally through conventional pressure-loading techniques (Gao et al., 2015). The XMT-mounted assembly for xenon saturation and core flooding is shown in Figure SB5. We load our core plug into the core holder, and at the bottom of this assembly is a brine-filled porous frit. The feed line is also brine filled. Fluid movement is prevented by closing the lower valve. At the top of the sample is an empty frit that will distribute the xenon gas across the sample face. Initially, the upper valve is closed and all components of the xenon supply are evacuated. This minimizes the amount of air without disrupting the core-plug saturation.

Because of the low permeability of the rock (a few millidarcys) the diffusion-controlled xenon saturation is a slow process. Modeling of the concentration profiles with a 1-D diffusion equation indicates that a typical diffusion coefficient is 1×10^{-10} m^2/s (1.55×10^{-7} $inch^2/s$). Consequently, we developed a procedure to speed the saturation. We first expose the sample to a higher pressure of xenon than needed to achieve the target attenuation. Then, after a few days, we lowered the pressure to the target value. (Note that the values in the figure are in linear adsorption coefficient, but these are easily translated

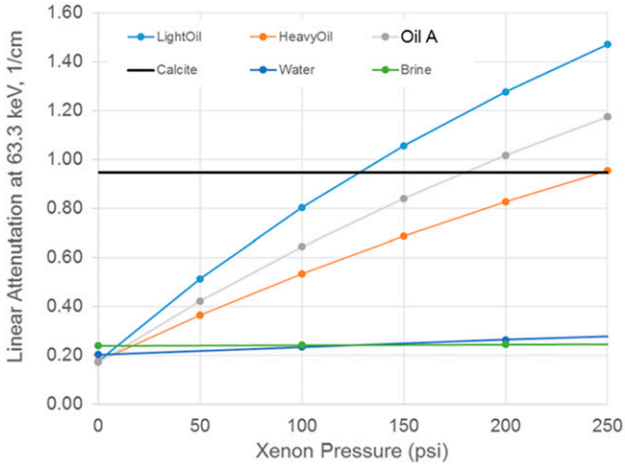

Figure SB3. At an assumed x-ray energy of 63.3 keV, this plot displays the calculated linear attenuation coefficients that result from equilibration of xenon gas with various components. Our experiments are typically conducted at pressures between 100 and 150 psi, (0.69–1.04 MPa) where the contrast between oil and water is high and the contrast with calcite is adequate. At some pressures, the contrast with calcite can diminish, making it difficult to resolve oil-filled pores from the calcite matrix; therefore, a careful consideration of the xenon pressure is important.

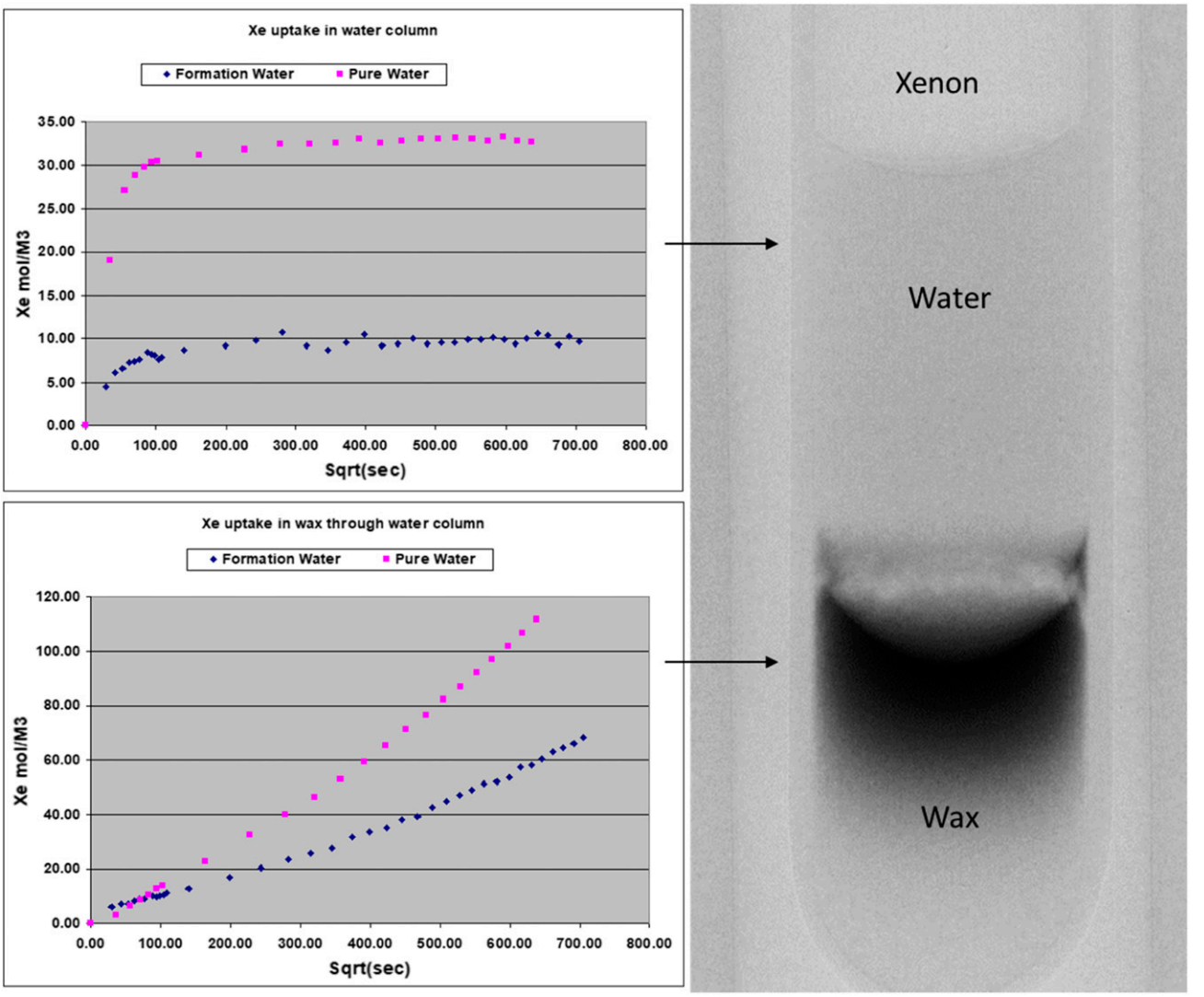

Figure SB4. To the right, the experimental setup; to the left are average concentrations measured along the centerline of synthetic three-dimensional reconstructions plotted as the square root of time (Sqrt). Note that the solubility in deionized water, i.e., pure water in figure (DI) is approximately three times that in formation water, i.e., saline water (FW), yet the kinetics are similar. Measurement shows that water impedes the xenon gas uptake by only a small amount, approximately 2 times. The difference in transport rates between DI and FW water is well approximated by the higher viscosity of the saline FW phase.

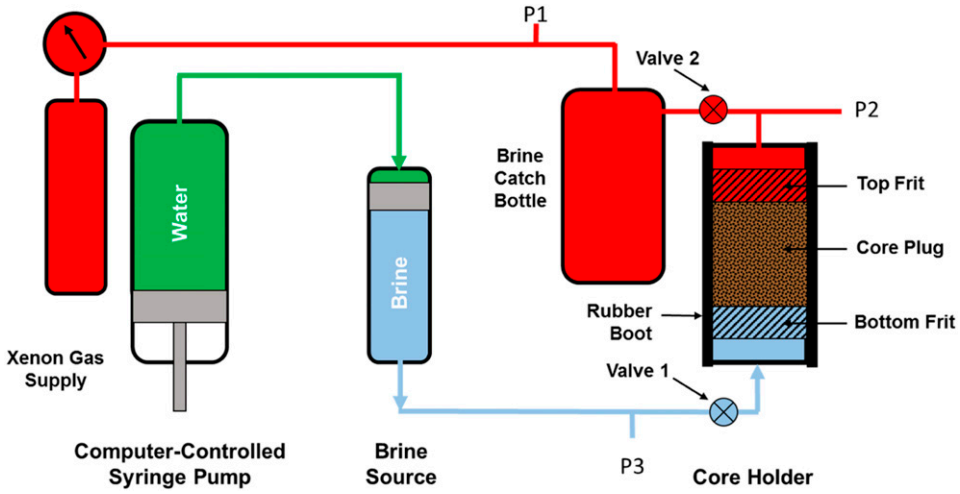

Figure SB5. Schematic of core-plug flooding with xenon saturation as implemented on the x-ray microtomography instrument. The xenon saturation is performed prior to brine flooding by subjecting the sample to a pressure (P1) of xenon gas, which diffuses into the sample from the top. The brine source is isolated from the sample through valve 1, which prevents fluid movement within the core plug during xenon filling. Upon saturation, the pressures at P2 and P3 are set equal and valve 1 opened; P3 is then increased to maintain a constant flow rate, typically 0.05 cm^3/min (0.00013 gal/min). Not shown are the two rotary cassettes, above and below the core holder, that allow its rotation within the x-ray beam.

to gas pressure through DiffTau imaging of the upper frit.) Using the 1-D diffusion model allows us to finely tune the timing for this manipulation. This results in a time savings of several weeks, which is more than that for simple diffusion at a fixed pressure.

REFERENCES CITED

Gao, B., J. Kralik, L. Vo, H. Shebl, R. Al Shehhi, A. Jawhari, M. Omar, and S. Fullmer, 2015, State of the art special core analysis program design and results for a Middle Eastern carbonate reservoir: Abu Dhabi International Petroleum Exhibition and Conference, Abu Dhabi, United Arab Emirates, November 9–12, 2015, SPE-177510-MS, 15 p.

Kharaka, Y. K., and D. J. Specht, 1988, The solubility of noble gases in crude oil at 25–100°C: Applied Geochemistry, v. 3, no. 2, p. 137–144, doi:10.1016/0883-2927(88)90001-7.

Potter, R. W. II, and M. A. Clynne, 1978, The solubility of the noble gases He, Ne, Ar, Kr, and Xe in water up to the critical point: Journal of Solution Chemistry, v. 7, no. 11, p. 837–844, doi:10.1007/BF00650811.

Nuclear magnetic resonance and x-ray microtomography pore-scale analysis of oil recovery in mixed-porosity carbonates

Hubert King, Michael Sansone, John Dunsmuir, Nicole Callen, Pavel Kortunov, Ye Xu, Antonio Buono, Bo Gao, and James Kralik

AAPG Bulletin, v. 104, no. 1 (January 2020), pp. 37–52

MODIFIED GOLDEN RATIO COMPUTERIZED TOMOGRAPHY SCANNING

Key Angle and Three-Dimensional Time Sequence Digital Subtraction

DiffTau Imaging

With the objective of capturing time-dependent changes, we created two specialized data collection routines. For the most rapidly varying conditions, we collect a sequence of radiographs taken at a fixed KeyAngle (DiffTau imaging). The angle is selected to provide an interpretable 2-D projection of some item or structure of interest, for example, parallel to bedding planes or fractures. Each radiograph is corrected for source intensity variation, and an absorbance image is calculated using the x-ray intensity from the initial reference image, Io, Figure SC1A.

Each image highlights changes with respect to the initial image throughout the sample. This feature is useful in monitoring fluid movement during sample flooding as well as monitoring xenon uptake of the sample during saturation. Data rates of up to one frame per minute are feasible, but much longer times (days) are also accessible.

The overall sample attenuation is not well represented by the areal average of the image. A major influence is that xenon uptake in the rubber sleeve is included in the signal. This background attenuation impacts our data. The radiographs are not corrected for beam hardening; consequently, the attenuation that is caused by xenon uptake at the cylindrical sample edges is over-represented. An approximation we use is that the correction is constant and equal for all DiffTau images, then we solve for a background contribution that correctly reproduces the oil recovery factor measured by the nuclear magnetic resonance. The correction is approximately one-third of the total attenuation and is equal for both samples

Impermeable Hassler sleeves and application of beam-hardening corrections obtained from the 3-D initial prexenon image can potentially correct these difficulties.

Golden Ratio Computerized Tomography Protocol

We use a modified version of the golden ratio (GR) scan protocol (Butler et al., 2011; Köhler, 2004) for tomographic data acquisition. Computerized tomography (CT) reconstructs a 3-D function from its projections taken from many different angles. In conventional CT, a set of projections is acquired using a small constant angular increment over the required angular range, commonly 360°. The data are complete only after the final projection is acquired. Thus, the time needed to complete a scan is fixed at the start of the experiment. If the scan stops prematurely, the set of projections is incomplete and produces reconstruction artifacts. Also, if the sample changes during the scan, the small angular increment from low to high angle over time produces projections of the initial structure at low angle and final structure at high angle. This temporal angular bias leads to reconstruction artifacts rather than a time average image.

The GR protocol (Köhler, 2004) uses a large angular increment defined by the GR, an irrational number $(1\pm\sqrt{5})/2 = 1.618$, times the scan range, typically 360°. This angular increment results in a nearly uniform sampling over the scan range within the first few projections. These few projections can be reconstructed, albeit at low resolution and signal-to-noise ratio. Because the GR increment produces a set of unique angles, subsequent projections improve the angular sampling and improve both the

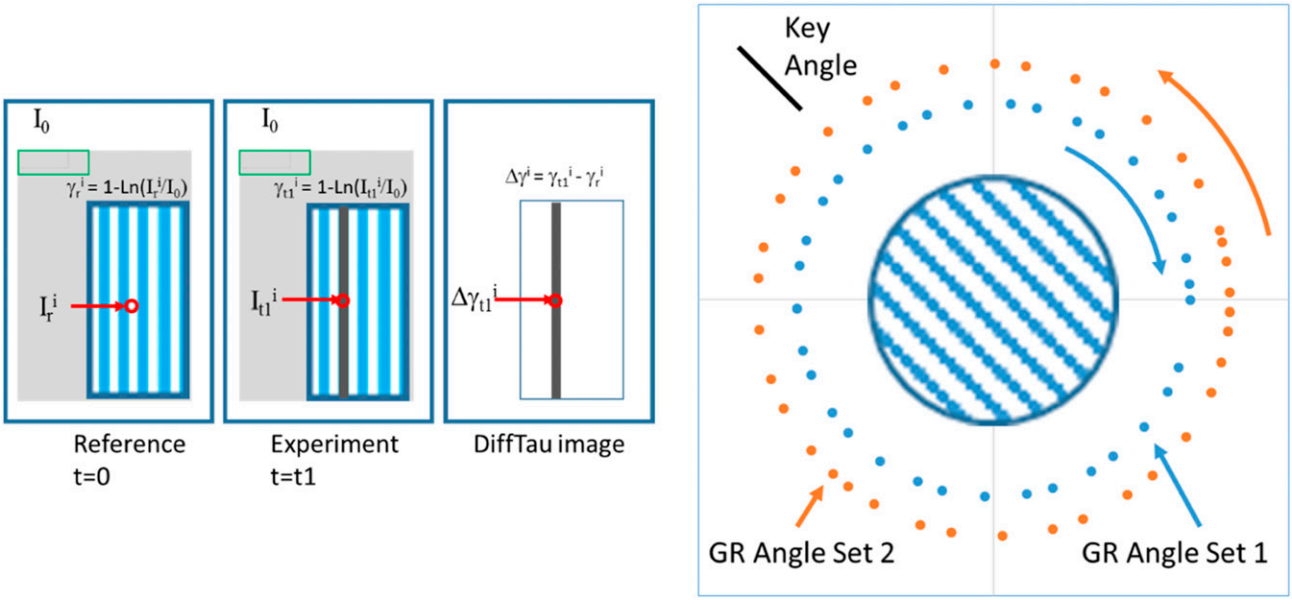

Figure SC1. (A) DiffTau imaging. Used in recording two-dimensional time-dependent changes. These occur, for example, during sample flooding or saturation with xenon. With the sample located in the core holder on the x-ray microtomography (XMT) unit, first a set of reference radiograph images is acquired. Following this, an experiment that results in changes in attenuation is initiated and a sequence of radiographs are acquired at a frequency that captures the changes. This can vary from seconds to days. To create a transcript of linear absorption coefficients, the images are all processed as shown in the final panel, with a time indicator for each image. The images are all georeferenced to the original reference image, and it is critical that the sample position can be registered to that starting point. This is most easily attained by having the sample remain on the XMT-mounting stage throughout. Alternatively, a digital adjustment is necessary. (B) Golden Ratio (GR) imaging. Used to create data sets for three-dimensional tomographic reconstruction. In addition, DiffTau imaging provided through KeyAngle images, one per GR angle set. Each GR angle set covers an entire 360° view of the sample, using sparse sampling. A low-resolution reconstruction is possible for less than one hour of data collection. These data help evaluate time evolution of the structure. For slowly evolving features, such as diffusion, multiple angle sets are combined. Upon reaching steady state, all subsequent GR angle sets are combined to produce the highest-resolution reconstruction.

resolution and signal-to-noise ratio. Over a long scan, many thousands of projections are acquired. Because only a few projections uniformly sample the specimen, nearly any subset of projections between two times during the scan can be reconstructed (Butler et al., 2011). Thus, the GR protocol can scan for an indefinite period of time and reconstruct 3-D images at time steps that can be selected either during the scan or after the scan has ended. Because nearby projection angles are spread out over time, GR produces a time-averaged image without angular bias.

The gas and confining pressure stainless steel tubes connected to the pressure cell used in this experiment do not permit continuous rotation. In addition, tracking changes in the sample during the CT scan is needed to monitor the progress of the experiment and is best accomplished using radiography from a repeatable KeyAngle. We, therefore, created a unique modified GR scan sequence.

Our GR procedure includes two modifications. The first generates a small sequence of GR angles, typically 36 angles between 0° and 360°, calculates each angle modulo 2π, and sorts the results in increasing order. The projections between 0° and 360° are acquired in approximately 10° angular increments. The next series of angles is then generated and sorted in decreasing order, and the projections between 360° and 0° are acquired. Thus, the sample oscillates between 0° and 360° in approximately 10° steps acquiring the GR angles slightly out of sequence. The connecting lines need to accommodate only 360° of rotation. The 10° steps significantly reduce the time spent rotating the sample and the resulting metal fatigue in the connecting lines. A nonuniform angular increment results from sorting the GR angles. This can cause problems for the reconstruction software program, and it is overcome by sorting the images within the

desired time slice back to the original GR order prior to reconstruction.

The second modification is to include a KeyAngle observation at each oscillation of the GR scan. Monitoring the progress of the experiment from the same angle produces a movie of the changes in the specimen from the same point of view. Using the GR projections to monitor changes is possible but requires a corresponding set of initial projections. These initial projections are obtained at the beginning of the experiment. If the sample holder is displaced, alignment of these initial images to match the displaced images is necessary.

Prior to starting the CT scan, a group of images is acquired at the KeyAngle at the maximum sampling rate of the CT scanner to monitor initial changes to the specimen. Once the CT scan starts, the KeyAngle measurement is inserted into each oscillation of GR angles. Thus, a 2-D radiographic record is created at a repeatable angle, initially with high temporal resolution (typically 20 s per frame), and during each oscillation of the CT scan at lower temporal resolution (typically 60 min per frame). The KeyAngle sequence can provide guidance for time slicing the GR data.

The modified GR protocol is illustrated in Figure SC1B. For truly static conditions, the highest resolution and signal-to-noise ratio are obtained by combining the entire group of GR subsets. For example, during core flooding, we stop the flow after a particular number of pore volumes and collect a full group of GR subsets. Approximately 3000 views are utilized.

To accommodate differential 3-D imaging, where changes in the sample are recorded by difference images between two 3-D volumes, voxel scale alignment is important. Barring equipment failure, our entire set of experiments are typically performed without removing the sample from the instrument. This has the deficit that our machine is occupied by a single experiment for several weeks. If necessary, we can align the volumes in postprocessing. This is best accomplished using markers applied to the sample that record translation and rotation of the entire sample volume. At the stresses of these experiments, differential strain of the sample is not important.

Nuclear magnetic resonance and x-ray microtomography pore-scale analysis of oil recovery in mixed-porosity carbonates

Hubert King, Michael Sansone, John Dunsmuir, Nicole Callen, Pavel Kortunov, Ye Xu, Antonio Buono, Bo Gao, and James Kralik

AAPG Bulletin, v. 104, no. 1 (January 2020), pp. 37–52

PROCEDURE FOR NUCLEAR MAGNETIC RESONANCE–GUIDED SEGMENTATION OF X-RAY MICROTOMOGRAPHY DATA

Using the NMR data on a fluid-saturated core plug, we obtain the overall porosity, ϕ_f. In addition, for data taken on the high-field NMR unit, proton spectroscopy can differentiate between oil and water; hence, we also separately obtain values of oil content and water content. Finally, through spectroscopic filtering, we can analyze the fluid-specific T_2 (spin–spin) relaxation times, obtaining estimates of the oil and water in micropores versus macropores. Summation of those latter data gives us percent microporosity. Together, these data constrain the x-ray microtomography segmentation.

POROSITY AND MICROPOROSITY CONSTRAINTS

In the first stage of this procedure, two attenuation thresholds, γ_{pore} and γ_{rock}, are identified that divide voxels into three populations: calcite, micropore, and macropore. Throughout this discussion the terminology γ will refer to linear attenuation coefficients with subscripts for the phases as follows: O = oil-filled pore; O_Xe = oil filled pore after xenon saturation; pore = fully-resolved pore; rock = fully-resolved calcite; W = water-filled pore.

After this calculation, the grayscale value of each voxel (ϕ_i) is rescaled so that for voxels with $\gamma_i > \gamma_{rock}$, $\phi_i = 0$, representing solid rock with zero porosity; for voxels with $\gamma_i < \gamma_{pore}$, $\phi_i = 1$, representing macropores with 100% porosity; and for voxels with $\gamma_{pore} \le \gamma_i \le \gamma_{rock}$, $\phi_i = (\gamma_{rock} - \gamma_i)/(\gamma_{rock} - \gamma_{pore})$, representing microporosity. The total porosity (Φ) and the percentage of microporosity of the sample (Φ_s) can then be calculated from the local porosity of each individual voxel.

Working on the distribution of linear attenuations for the fluid-saturated sample and making the approximation that oil and water have the same attenuation ($\gamma_{fluid} = \gamma_W = \gamma_O$), we use two constraints to solve for γ_{pore} and γ_{rock}.

The Φ is calculated using

$$\Phi = \frac{\sum \phi_i}{N} = \sum \frac{n \in (\gamma_i \le \gamma_{pore})}{N} + \sum \frac{\frac{\gamma_{rock} - \gamma_i}{\gamma_{rock} - \gamma_{pore}} \in (\gamma_{rock} < \gamma_i < \gamma_{pore})}{N} \quad (1)$$

where N is the total number of voxels in the sample. The first term on the right is the total open-pore voxels, and the second term counts the number of partially open voxels, weighting the contribution of

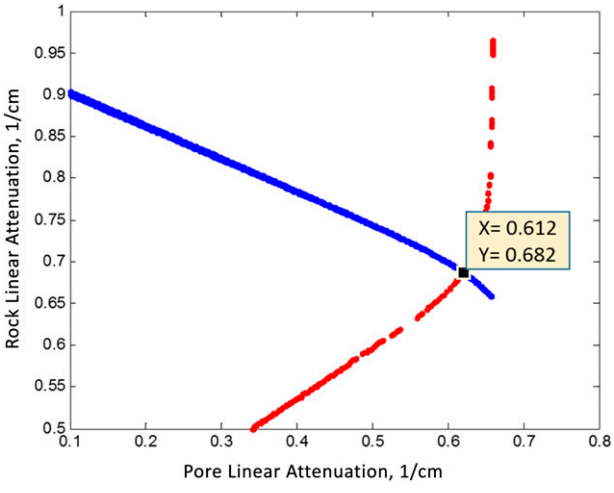

Figure SD1. Determination of upper (γ_{rock}) and lower (γ_{pore}) cutoff for the linear attenuation histogram. The blue line indicates those solutions satisfying the porosity constraint and the red line indicates solutions for the microporosity constraint. Their intersection gives the required quantities.

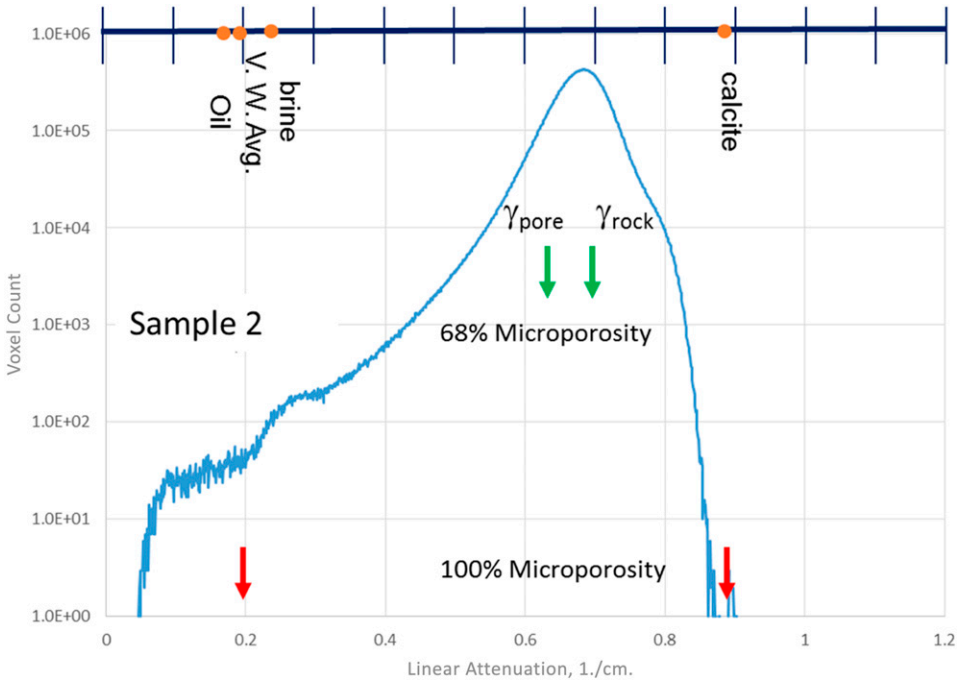

Figure SD2. Comparison of histogram of linear attenuation values with the calculated γ_{pore} and γ_{rock} values. Note that the values are considerably shifted from the pure component values indicated by the red arrows. The calculated linear attenuation values are displayed on the upper axis. The volume weighted average (V.W. Avg.) is simply the weighted average of the pore-filling components. We discuss in the next section how finite resolution causes the shift from pure component values.

each by the selected γ_{pore} and γ_{rock} values. The Φ_S is then calculated using

$$\Phi_S = 1 - \frac{\sum n \in (\gamma_n \le \gamma_{pore})}{N\Phi} = 1 - \frac{N_{open}}{N\Phi} \quad (2)$$

where N_{open} is the number of macropore voxels with 100% porosity. Under the constraints of Φ and microporosity values from the NMR analysis, these two equations give γ_{pore} and γ_{rock}. We do not expect that the attenuation thresholds will correspond to the calculated linear attenuation coefficients of the pure components. Because of finite voxel size, the thresholds are shifted to accommodate the gradients in attenuation near grain and pore boundaries. We show an example below using a digital rock simulation.

Our first step in NMR-guided segmentation is performed on the base 3-D image, i.e., the linear attenuation values histogram measured from the fluid-filled rock. We analyze those values seeking the simultaneous solution of equations 1 and 2 to obtain values for γ_{pore} and γ_{rock}. This calculation may be carried out as a grid search in γ_{pore}–γ_{rock}, as illustrated in Figure SD1, or solved directly through two consecutive 1-D searches. In the grid search, we first select pairs of values that give the correct Φ, generating a line in the γ_{pore}–γ_{rock} space. We then generate a second line corresponding to the target percent microporosity. At the intersection point of these two lines is the desired solution. A sampling grid of $\Delta = 0.001$ cm^{-1} is sufficient.

We consider here, for example, sample 2, which has a porosity of 24.8% with 68% micropores. The results of the grid search are displayed in Figure SD1, where the intersection of the two constraining equation solutions gives the desired thresholds.

FINITE RESOLUTION EFFECT ON THRESHOLD VALUES

As is clear from Figure SD2, although the γ_{rock} and γ_{pore} values correctly reproduce the porosity and microporosity, they are not equal to those of the pure components. Furthermore, if we were to apply the pure component values to Figure SD2, we would find that the solution to the equations would give the

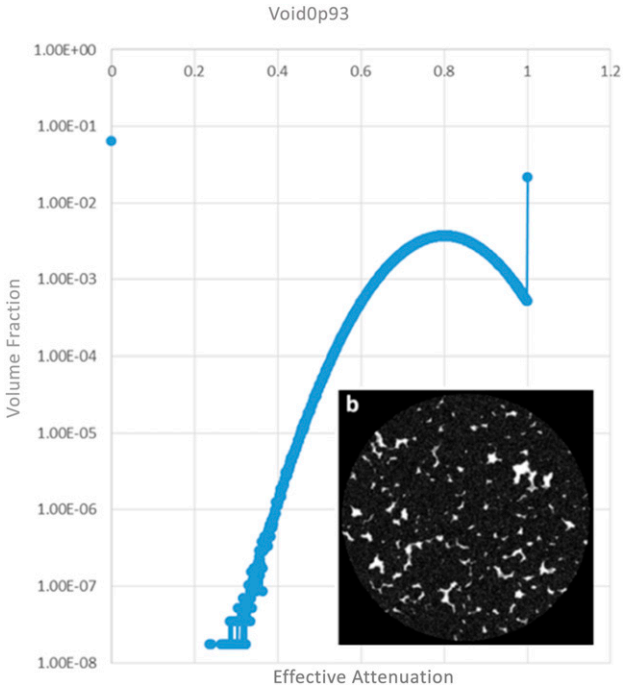

Figure SD3. Histogram of effective linear attenuation values for a digital rock having 25.4% porosity with 74% microporosity.

correct porosity but only for 100% microporosity. Also, this would give an unrealistic low number of voxels consisting of pure calcite. This effect is caused by finite resolution for the XMT data as we now demonstrate.

Consider the image in Figure SD3, which is taken from a digital rock model for grain stones from Xu et al. (2017).

If we degrade the resolution of this digital model by averaging adjacent voxels, we approximate how a finite resolution affects the XMT data. We reduce the resolution by a factor of two and find that the histogram is significantly altered. Not surprisingly, many fewer voxels equal zero or one. This is displayed in Figure SD4.

We now apply our analysis to recover the correct porosity and microporosity. The resulting values of γ_{rock} and γ_{pore} are 0.921 and 0.434, respectively, which are considerably different from their original values of 1 and 0, respectively. However, when we apply these values to the degraded resolution digital rock volume, we correctly recover the porosity (25.2%) and microporosity (74%). Mathematically, one can see that what has occurred is that the original

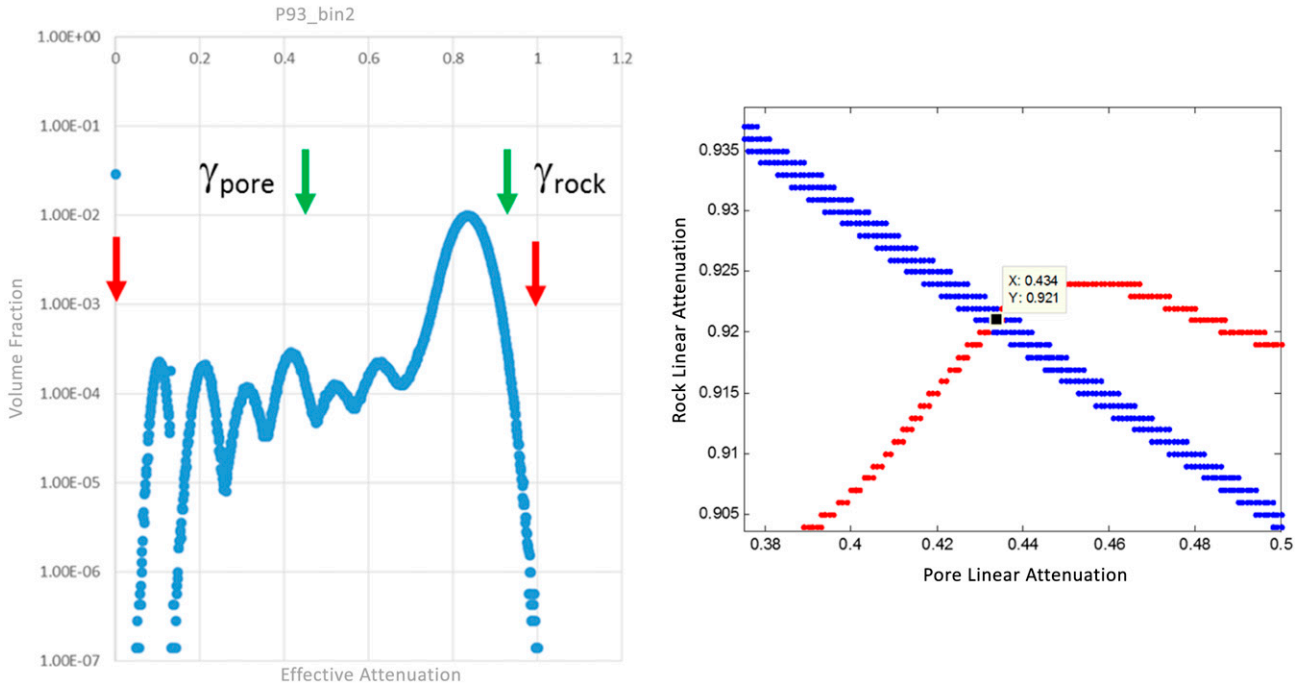

Figure SD4. (Left) Effect on histogram of reducing resolution by factor of two. Note reduction of zero and one values representing the pure components of pore and calcite. Oscillations within histogram are artifacts of nonrandom distribution of microporosity grayscale levels because of finite size. Analysis under constraint of known porosity and microporosity results in values of γ_{rock} and γ_{pore}. These values successfully recover the original digital rock values from this lower-resolution image.

sharp boundary between the two regions has been blurred by the reduced resolution, and this technique approximates where to draw the new boundary to recover the correct volume of the regions.

OIL–WATER CONSTRAINTS

The final step in segmentation aims to identify the oil filling of each voxel. For this, we combine the base image and one for xenon-saturated oil. The difference between the two images is directly proportional to the amount of oil in the sample.

With xenon-saturated oil, the attenuations of oil and water are no longer equal, i.e., $\gamma_{O\_Xe} > \gamma_W$. Because the xenon uptake of water is small, we can safely neglect this effect. We obtain a new expression for the attenuation of each voxel and express that as the difference in linear attenuation. We write that attenuation in recognition that in this procedure we will partition our rock into three components (calcite, oil, and water):

$$\Delta\gamma_i = \phi_i \phi_i^O (\gamma_{O\_Xe} - \gamma_O) \quad (3)$$

where ϕ_i is the voxel porosity derived by the first step of the NMR segmentation, that is, $1 \geq \phi_n \geq 0$. The new variable, ϕ_i^O, is the fraction of oil filling that pore, with the remainder being water.

Using the NMR results, we have a direct measure of the fraction of Φ occupied by oil and water. We now use that constraint to select, by recursive calculation, a value for $(\gamma_{O\_Xe} - \gamma_O)$ that will satisfy the following equations:

$$\phi_{NMR}^O = \sum \phi_i \phi_i^O \quad (4)$$

$$\phi_{NMR}^W = 1 - \sum \phi_i \phi_i^O \quad (5)$$

This allows the selection of a unique linear attenuation threshold for $\gamma_{O\_Xe} - \gamma_O$ that segments the XMT image under constraint to equal the volume fractions oil and water imposed by NMR. Using all three linear attenuation threshold values, we now obtain a voxel-scale distribution of oil and water throughout the sample. For consistency, these same linear attenuation thresholds are applied throughout the course of the flooding experiments. As a check on the accuracy, we compare the oil and water determinations by XMT and NMR at the conclusion of the experiment, finding good agreement.

REFERENCES CITED

Xu, Y., Q. Li, and H. E. King, 2017, Modeling oil recovery for mixed macro-and micro-pore carbonate grainstones: Scientific Reports, v. 7, no. 1, 11 p., doi:10.1038/s41598-017-09507-4.